Transport across a carbon nanotube quantum dot contacted with ferromagnetic leads: Experiment and nonperturbative modeling

Alois Dirnaichner* and Milena Grifoni
Institute for Theoretical Physics, University of Regensburg, 93040 Regensburg, Germany

Andreas Prüfling, Daniel Steininger, Andreas K. Hüttel, and Christoph Strunk
Institute for Experimental and Applied Physics, University of Regensburg, 93040 Regensburg, Germany
(Received 6 February 2015; revised manuscript received 9 April 2015; published 6 May 2015)

We present measurements of tunneling magnetoresistance (TMR) in single-wall carbon nanotubes attached to ferromagnetic contacts in the Coulomb blockade regime. Strong variations of the TMR with gate voltage over a range of four conductance resonances, including a peculiar double-dip signature, are observed. The data are compared to calculations in the "dressed second order" (DSO) framework. In this nonperturbative theory, conductance peak positions and linewidths are affected by charge fluctuations incorporating the properties of the carbon nanotube quantum dot and the ferromagnetic leads. The theory is able to qualitatively reproduce the experimental data.

DOI: 10.1103/PhysRevB.91.195402 PACS number(s): 85.75.−d, 73.63.Fg, 75.76.+j, 72.25.−b

I. INTRODUCTION

Controlling electronic spin in nano-scale circuits is a long-lasting challenge on the way to fast-switching, energy-efficient building blocks for electronic devices. To this end, spin-dependent transport properties have been investigated in a wealth of low-dimensional systems, e.g., mesoscopic magnetic islands [1], 2DEGs [2], InAs nanowires [3], graphene [4], and fullerenes [5]. Carbon nanotubes (CNTs), being thin, durable and high-throughput wiring, allow coherent transport of electronic charge and spin and are promising candidates for future spintronics applications [6]. While control and scalability of CNT-based nanocircuits still pose significant challenges, devices where single carbon nanotubes (CNTs) are contacted to ferromagnetic leads can be produced with standard lithography methods: spin valve experiments were performed on single-wall [7–10] (SWCNT) and multiwall [11–15] carbon nanotubes in various electron transport regimes. In most cases, a spatially confined quantum dot is coupled to ferromagnetic electrodes. Electronic transport across CNT quantum dots can take place in different regimes: depending on the relative magnitude of coupling strength, temperature and charging energy, this ranges from an opaque Coulomb-blockade regime [16–19], to an intermediate coupling regime with lead induced energy level shifts [20–22], to a strongly correlated Kondo regime [23–26]. For highly transparent contacts, in contrast, the dot behaves essentially like an electronic wave guide [27,28].

In our work, we focus on the conductance of a carbon nanotube quantum dot weakly coupled to ferromagnetic contact electrodes, recorded for parallel (G_p) and antiparallel (G_ap) contact magnetization, respectively. G_p and G_ap define the so-called tunneling magnetoresistance (TMR) [27,29]: $\mathrm{TMR} = (G_\mathrm{p}/G_\mathrm{ap}) - 1$. Experimentally, the TMR has been shown to be strongly gate dependent [7,30]. We report on shifting and broadening of conductance peaks resulting in specific dip-peak and dip-dip sequences in the TMR gate dependence. Our data covers a range of four Coulomb resonances with extremal TMR values of -20% to $+180\%$.

The pronounced resonant structure of the conductances G_p and G_ap leads to large TMR values if the positions and widths of the resonances depend on the magnetization configurations p and ap. Thus, various mechanisms have been proposed which induce a shift of the energy levels of the quantum dot, and thus the of the resonance peaks, depending on the magnetization of the contacts. Those are spin-dependent interfacial phase shifts [7] or virtual charge fluctuation processes [21,25]. The effect of spin polarized leads on the resonance width have been described in Ref. [31] for a resonant single level junction. Interestingly, a negative TMR is predicted for asymmetric couplings to the leads. An attempt to account for broadening in the presence of Coulomb interactions was discussed within a self-consistent approach based on the equation of motion (EOM) technique [20]. The EOM was applied to model TMR data reported for a SWCNT [7] for a model with spin-dependent interfacial phase shifts.

Here, we discuss a transport theory which naturally incorporates the effects of spin polarized leads on the position and width of conductance resonances in the presence of strong Coulomb interactions. It is an extension of the so-called dressed second-order (DSO) transport theory, recently developed for normal leads [22], to the case of spin-polarized contacts. This theory accounts for energy renormalization and broadening of the peaks in linear conductance due to charge fluctuation processes. We show that the charge fluctuations also affect transport through excited states in the nonlinear conductance regime. This observation is in agreement with previous reports on tilted co-tunneling lines in CNT quantum dots [32]. A qualitative agreement with the experimental findings is obtained.

This paper is structured as follows. We first present the measurement details and experimental data in Sec. II. In Sec. III, we introduce the so-called dressed second order theory (DSO) [22] in the reduced density matrix transport framework and address its implications on nonlinear conductance and TMR. Finally, in Sec. IV, we provide a comparison between

*alois.dirnaichner@ur.de

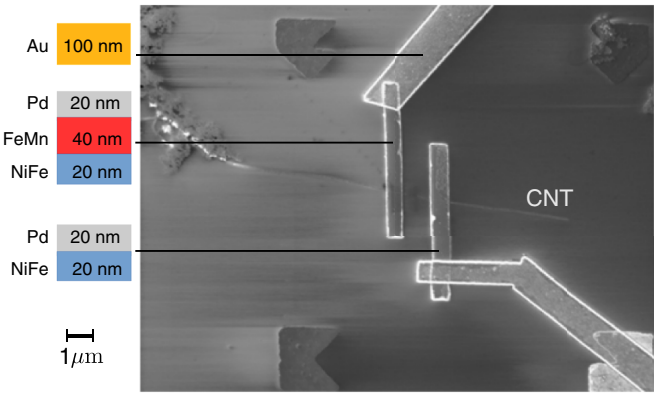

FIG. 1. (Color online) SEM picture of a chip structure similar to that of the measured device. A carbon nanotube on a positively doped silicon substrate capped with 500 nm SiO_2 is contacted by two permalloy stripes, one of which is exchange-biased by a FeMn layer. On top, the stripes are protected by palladium. Gold is used for the bond pads and the connections to the nanotube contacts.

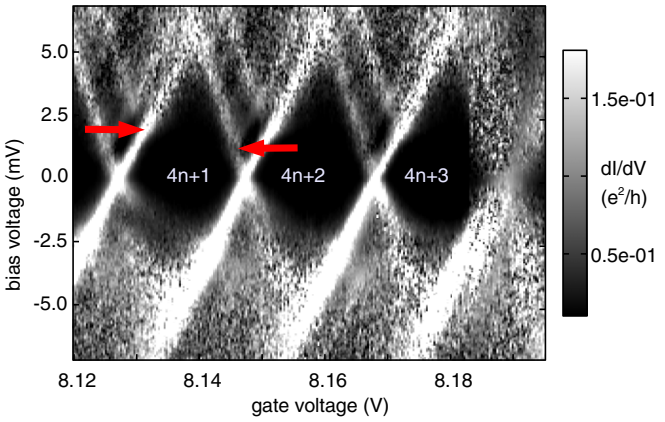

FIG. 2. (Color online) Differential conductance vs bias and gate voltage of a selected region measured at 300 mK and $B = 0$. The numbers in the Coulomb blockade regions denote the number of electrons in shell n on the quantum dot. Arrows indicate the first excited state crossing the source (left) and drain (right) lines in the vicinity of the state with one extra electron ($N = 4n + 1$).

experimental data and results from the DSO and draw our conclusions in Sec. V.

II. EXPERIMENT

A. Sample preparation

For the purpose of measuring TMR in CNTs, one needs to interface the nanotube to two ferromagnetic contacts with a different switching field. The conductance, being sensitive to the magnetization in the leads, changes when the polarization of one of the contacts is reversed by an external magnetic field. It has been shown that NiFe is well suited as a material for the electrodes of CNT spin valves [33]: the alloy shows a distinct switching behavior as a function of the applied magnetic field and the interface transparency between NiFe and the CNT is comparable to that of Pd. The structure of one of the devices we realized for this purpose is shown in Fig. 1. On an oxidized silicon substrate (500 nm SiO_2) a carbon nanotube is grown by chemical vapor deposition. The nanotube is located by atomic force microscopy and two NiFe (80:20) leads, 20 nm in thickness, are deposited at a distance of 1 μm on top of the nanotube by sputtering. On one of the two contacts, 40 nm of antiferromagnetic FeMn (50:50) is sputtered to bias the magnetization of the underlying NiFe contact. The hysteresis loop of this contact is expected to be shifted with respect to the pure NiFe contact by virtue of the exchange bias effect [34]. A 20 nm protective layer (Pd) covers the leads from the top. The switching of the exchange biased contacts was confirmed independently prior to the measurement using superconducting quantum interference device (SQUID) and vibrating sample magnetometer techniques.

B. Measurement

An electronic characterization of the quantum dot at 300 mK and at zero magnetic field shows a regular Coulomb blockade behavior (Fig. 2). The data yield a gate conversion factor $\alpha = 0.29$ and a charging energy of $E_c = 6.1$ meV [see Eq. (1)]. The sample does not exhibit a clear fourfold symmetry in the peak height or peak spacing as expected for a carbon nanotube quantum dot. Consequently, we are not able to label the Coulomb blockade regions with a value of the electronic shell filling n in a definite way. The assignment of the number of electrons to the experimental data in Fig. 2 is done in agreement with the theoretical predictions in Sec. III E.

Having a closer look at Fig. 2, we can identify an excited state transition at 1.4 meV parallel to the source line (left arrow) and at ~1.8 meV parallel to the drain line (right arrow). The energy scale of this excitation stays approximately constant over a range of at least six resonances, as can be seen from measurements over a broader gate range. The quantization energy $\epsilon(n)$ of a CNT shell n is a direct consequence of the electron confinement along the nanotube. It yields a mean level spacing $\epsilon_0 = \epsilon(n+1) - \epsilon(n) \propto \hbar v_F/\pi L$, where L is the CNT length. It is thus reasonable to identify the first excitation with the confinement energy ϵ_0 equivalent to a lateral confinement of 1.1 μm for a Fermi velocity of 800 km/s [35], a value close to the contact spacing of 1 μm. The asymmetry of the line spacing with respect to source and drain suggests a gate-dependent renormalization [32] of the CNT many-body addition energies in the presence of ferromagnetic contacts. We show in Sec. III D that this can be a direct consequence of charge fluctuations in the presence of contact magnetization.

Electron transport measurements at 300 mK show a significant switching behavior. In Fig. 3, the conductance across the CNT quantum dot is plotted against the magnetic field directed parallel to the stripes, i.e., along their easy axis, as indicated in the inset to the figure. The steps in the signal can be interpreted as the magnetization reversal of the contacts, as sketched in the figure. Sweeping the magnetic field from negative (−100 mT) to positive values, one of the contacts switches at $H = H_{s,u}$, resulting in a configuration with antiparallel polarization of the majority spins of the two contacts. This results in a drop of the conductance signal. Upon increasing the field further, the second contact is supposed to switch and the conductance should recover. The second switching event was not observed in the present sample.

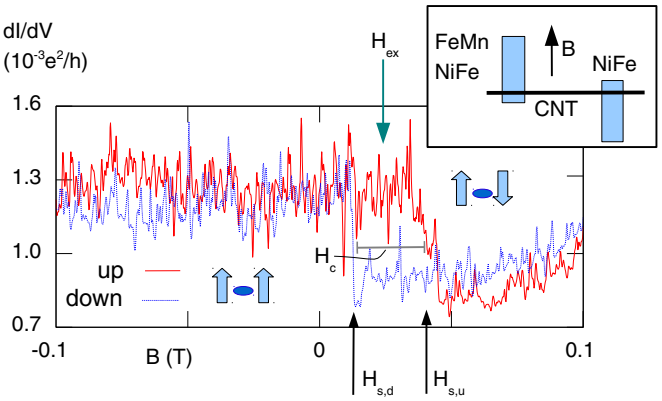

FIG. 3. (Color online) Differential conductance plotted vs magnetic field at $V_g = 8.1737$ V, $V_b = 0$ and 300 mK. The solid red curve was recorded with increasing field, the dashed blue curve with decreasing field. Small pictograms indicate possible orientations of the majority spins in the contacts. The switching of one of the two contacts at $H_{s,u/d}$ is highlighted with arrows at the bottom for both sweep directions. The coercive field is indicated by H_c and the exchange bias by H_{ex}. (Inset) Orientation of the external field B with respect to the CNT and the leads.

Sweeping back from positive to negative field, the conductance recovers at $H_{s,d}$. The two values $H_{s,d/u}$ characterize a hysteresis loop with a coercive field $H_c = H_{s,u} - H_{s,d}$ and an exchange bias $H_{ex} = (H_{s,u} + H_{s,d})/2$. At $B = 0$, the two contacts are always in a parallel configuration, because the coercive field of the switching contact is smaller than the exchange bias.

Measurements of the conductance performed at zero magnetic field require $\Delta t^{\text{fast}} \sim 100$ ms per data point and will be called the *fast* measurements in the following. Contrarily, in *slow* measurements, each conductance data point is obtained from magnetic field sweeps with a duration of $\Delta t^{\text{slow}} \sim 20$ minutes at constant gate voltage (compare Fig. 3). We then identify H_s from a step in the conductance signal and take the average over 100 points on either side of the step to extract the conductance in the parallel and antiparallel configuration, respectively. This is repeated for 250 values of the backgate potential in the range between 8.126 and 8.201 V. In Fig. 4,

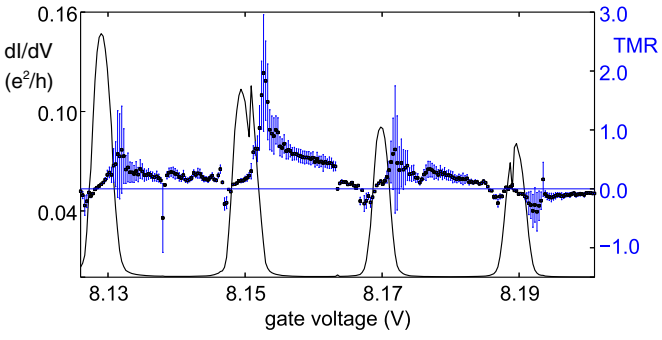

FIG. 4. (Color online) Differential conductance and TMR as a function of gate voltage measured over four resonances (*slow* measurement, see text). The conductance is measured at parallel polarization of the contacts. The TMR graph shows a dip-peak sequence over the first two resonances and a qualitatively different double-dip feature at the last two.

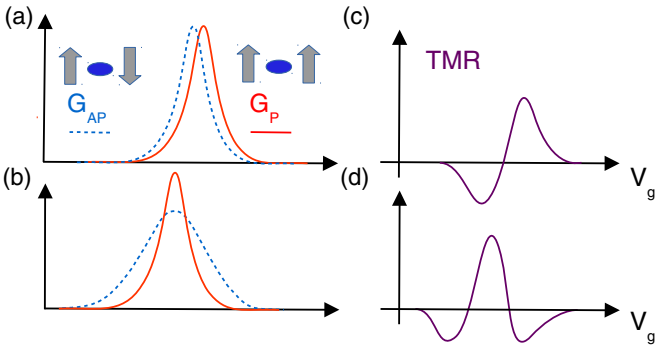

FIG. 5. (Color online) (Left) Schematic drawing of the lead induced, polarization dependent, modification of position (a) and width (b) of a peak in the conductance across a quantum dot as a function of the gate voltage. (Right) As a consequence of the level shift (a) and level broadening (b), the corresponding TMR signal exhibits a characteristic dip-peak (c), or dip-peak-dip (d) feature.

the TMR as a function of gate voltage is shown together with the conductance at parallel contact polarization. In this *slow* measurement, we obtain conductance peaks with a height of $0.15e^2/h$ and a full width at half maximum (FWHM) of $\Gamma \sim 0.7$ meV. Comparing these values to a height of $0.3e^2/h$ and a width of 0.4 meV obtained from the *fast* measurement at $B = 0$ we conclude that the peak conductance in the data from the *slow* measurement is substantially suppressed. We will discuss this deviation in Sec. IV. It is remarkable that besides huge positive (180%) TMR values, negative regions occur prior to the peak in the TMR curve in the first two resonances, while for the last two, the value drops again, forming two dips in sequence. Again this will be discussed in more detail in Sec. IV.

III. THEORETICAL MODELING

We proceed by presenting a theoretical framework capable to reproduce the transport data from the previous section. In particular, the connection between the theory and the resulting shape of the TMR curve will be discussed in detail. In order to be able to account for a gate dependence of the TMR, the transport theory should be able to incorporate the influence of the ferromagnetically polarized leads on the positions of the linear conductance maxima as well as on the width of the conductance peaks.

Noticeably, the commonly used perturbative description of the Coulomb resonances predicts temperature broadened peaks and maxima whose positions are solely determined by the isolated quantum dot spectrum implying a constant, positive TMR [21].

A transport theory accounting for charge fluctuations nonperturbatively was shown to shift the quantum dot energy levels depending on the magnetization configuration of the leads [21]. The qualitative effect of the renormalization is depicted in Fig. 5(a): The peak in the conductance G_p in presence of leads with parallel spin polarization is shifted with respect to the one in G_{ap}, the conductance in the antiparallel case. This shift yields a characteristic dip-peak feature in the TMR signal, similar to what was observed in Ref. [7]. Yet, this

theory cannot account for the double-dip like TMR signatures visible in our data (see Fig. 4, $V_g \sim 8.19$ and ~ 8.17 V). These require additionally a change of the resonance linewidth when switching from the parallel to the antiparallel configuration, as shown in Fig. 5(b) and also observed lately in Ref. [30].

In the following, we discuss how to theoretically account for broadening and renormalization effects, to lowest order in the coupling Γ, within the recently proposed "dressed second order approximation" (DSO). The DSO has been discussed in Ref. [22] for the single impurity Anderson model with normal metal leads, where it has been shown to correctly capture the crossover from thermally broadened to tunneling broadened conductance peaks. Here we present its generalization to a multilevel system coupled to ferromagnetic leads.

A. Hamiltonian

We treat the system as an isolated quantum dot coupled to metallic leads. The Hamiltonian of such a system reads $\hat{\mathrm{H}} = \hat{\mathrm{H}}_\mathrm{R} + \hat{\mathrm{H}}_\mathrm{D} + \hat{\mathrm{H}}_\mathrm{T}$. Here,

$$\hat{\mathrm{H}}_\mathrm{R} = \sum_{l\sigma\mathbf{k}} \epsilon_{l\sigma\mathbf{k}} \hat{c}^\dagger_{l\sigma\mathbf{k}} \hat{c}_{l\sigma\mathbf{k}}$$

is the Hamiltonian of an ensemble of noninteracting electrons in the leads $l = \mathrm{s/d}$ with wave vector $\mathbf{k}$ and spin σ. The operator $\hat{c}_{l\sigma\mathbf{k}}$ ($\hat{c}^\dagger_{l\tau\sigma k}$) annihilates (creates) an electron with energy $\epsilon_{l\sigma\mathbf{k}}$. The second part,

$$\hat{\mathrm{H}}_\mathrm{D} = \frac{1}{2} E_c \hat{\mathrm{N}}^2 + \sum_{n\tau\sigma} \left[\epsilon(n) + \tau\sigma \frac{\Delta_\mathrm{SO}(n)}{2} \right] \hat{\mathrm{N}}_{n\tau\sigma} - e\alpha V_g \hat{\mathrm{N}} + \hat{\mathrm{H}}^{\mathrm{P/A}}_\mathrm{ext}, \quad (1)$$

describes the electrons on the CNT quantum dot in terms of the quantum numbers n (shell), spin σ and valley τ. Here, we used $\hat{\mathrm{N}}_{n\tau\sigma} = \hat{d}^\dagger_{n\tau\sigma} \hat{d}_{n\tau\sigma}$, with the fermionic dot operator $\hat{d}_{n\tau\sigma}$ and $\hat{\mathrm{N}} = \sum_{n\tau\sigma} \hat{\mathrm{N}}_{n\tau\sigma}$, the total dot occupation. For our purposes, it is sufficient to account for Coulomb interaction effects in terms of a capacitive charging energy E_c. Short-range exchange contributions are neglected here. The symbols τ and σ represent the eigenvalues ± 1 of the states with quantum numbers K, K' and $\uparrow, \downarrow$, respectively. In the CNT, a nonzero spin-orbit coupling Δ_SO can lead to the formation of degenerate Kramer pairs [26]. Notice that, for simplicity, a valley mixing contribution is not included in Eq. (1), as it would not affect the main conclusions drawn in this work. Hence the valley degree of freedom is a good quantum number to classify the CNT's states [36]. The next to last part of the Hamiltonian $\hat{\mathrm{H}}_\mathrm{D}$ models the effect of an electrostatic gate voltage V_g scaled by a conversion factor α. Finally, $\hat{\mathrm{H}}^{\mathrm{p/a}}_\mathrm{ext}$ accounts for external influences on the dot potential, e.g., stray fields from the contacts and the external magnetic field used to switch the contact polarization.

The ground states of shell n have $4n + a$ ($0 \leqslant a \leqslant 3$) electrons and will in the following be characterized by the quantum numbers of the excess electrons with respect to the highest filled shell $n - 1$. For instance, the quantum dot state labeled by $|K\uparrow; n\rangle$ contains $4n$ electrons plus one additional electron in the $(K, \uparrow)$ state. Including states with $4n - 1$ and $4n + 5$ electrons we end up with six ground states with different degeneracies (see Table I, left column). In total, we consider a Fock space of dimension 24 if the fourfold degeneracy is not lifted by a sufficiently large spin-orbit coupling Δ_SO. The extra states with occupation $4n - 1$ and $4n + 5$ are included to allow for charge fluctuations in and out of the shell n under consideration. Conversely, for large enough spin-orbit coupling the dimension of the Fock space is reduced to 10, see Table I, right column. Judging from the stability diagram in Fig. 2 and from data over a greater gate range where we see no twofold pattern in the spacing of the excited state lines, we consider the configuration on the left side in Table I to be more likely. For a compact notation, the shell number will in the following be neglected from the state ket if not necessary.

TABLE I. The set of allowed electronic ground states C of the CNT with N electrons for large (right) and small (left) spin-orbit coupling Δ_SO. The degeneracy of the configuration depends on the magnitude of Δ_SO. In the first column, the excess electron number $N_\mathrm{rel} = N - 4n$ is reported with respect to the number $4n$ of electrons in the filled $(n-1)$-th shell.

N_rel	$\Delta_\mathrm{SO} \leqslant \max\{k_B T, \gamma_0\}$	$\Delta_\mathrm{SO} \gg \max\{k_B T, \gamma_0\}$
-1	$\|K\uparrow, K\downarrow, K'\uparrow; n-1\rangle$ $\|K\uparrow, K\downarrow, K'\downarrow; n-1\rangle$ $\|K\uparrow, K'\uparrow, K'\downarrow; n-1\rangle$ $\|K\downarrow, K'\uparrow, K'\downarrow, n-1\rangle$	$\|K\uparrow, K\downarrow, K'\uparrow; n-1\rangle$ $\|K\uparrow, K\downarrow, K'\downarrow, n-1\rangle$
0	$\|n\rangle$	$\|n\rangle$
1	$\|K\uparrow; n\rangle$ $\|K\downarrow; n\rangle$ $\|K'\uparrow; n\rangle$ $\|K'\downarrow; n\rangle$	$\|K\uparrow; n\rangle$ $\|K\downarrow; n\rangle$
2	$\|K\uparrow, K\downarrow; n\rangle$ $\|K\uparrow, K'\uparrow; n\rangle$ $\|K\uparrow, K'\downarrow; n\rangle$ $\|K\downarrow, K'\uparrow; n\rangle$ $\|K\downarrow, K'\downarrow; n\rangle$ $\|K'\uparrow, K'\downarrow; n\rangle$	$\|K\uparrow, K\downarrow, n\rangle$
3	$\|K\uparrow, K\downarrow, K'\uparrow; n\rangle$ $\|K\uparrow, K\downarrow, K'\uparrow; n\rangle$ $\|K\uparrow, K'\uparrow, K'\downarrow; n\rangle$ $\|K\downarrow, K'\uparrow, K'\downarrow; n\rangle$	$\|K\uparrow, K\downarrow, K'\uparrow; n\rangle$ $\|K\uparrow, K\downarrow, K'\downarrow; n\rangle$
4	$\|n+1\rangle$	$\|n+1\rangle$
5	$\|K\uparrow; n+1\rangle$ $\|K\downarrow; n+1\rangle$ $\|K'\uparrow; n+1\rangle$ $\|K'\downarrow; n+1\rangle$	$\|K\uparrow; n+1\rangle$ $\|K\downarrow; n+1\rangle$

Quantum dot and metallic leads are coupled perturbatively by a tunneling Hamiltonian

$$\hat{\mathrm{H}}_\mathrm{T} = \sum_{l\mathbf{k}n\sigma\tau} T_{l\mathbf{k}n\sigma\tau} d^\dagger_{n\sigma\tau} c_{l\mathbf{k}\sigma} + \mathrm{H.c.}, \quad (2)$$

with a tunnel coupling $T_{l\mathbf{k}n\sigma\tau}$ generally dependent on the quantum numbers of both leads and quantum dot. In the following, for simplicity, we assume that $T_{l\mathbf{k}n\sigma\tau} = T_l$.

B. The reduced density matrix within the dressed second-order (DSO) approximation

We describe the state of our system by the reduced density matrix $\hat{\rho} = \mathrm{Tr_R}\{\hat{\rho}_\mathrm{tot}\}$, obtained by tracing over the possible configurations of states in the reservoirs, assuming that they are in thermal equilibrium. For the quantum dot itself, we suppose that it reaches a steady state characterized by $\dot{\hat{\rho}} = 0$.

The corresponding stationary Liouville equation reads [22]

$$0 = -\mathrm{i}\sum_{aa'}\delta_{ab}\delta_{a'b'}(E_a - E'_a)\rho_{aa'} + \sum_{aa'}K^{aa'}_{bb'}\rho_{aa'}, \quad (3)$$

in terms of matrix elements $\rho_{ab} = \langle a|\hat{\rho}|b\rangle$ of $\hat{\rho}$ in the eigenbasis of the quantum dot. The superoperator K connects initial states $|a\rangle$, $|a'\rangle$ to final states $|b\rangle$ and $|b'\rangle$ at a certain order in the perturbation $\hat{\mathrm{H}}_\mathrm{T}$.

The calculation of the kernel elements is performed along the lines of Ref. [22]. As an example, the element connecting the states $|b\rangle$, $|b'\rangle = |b\rangle$ and $|a\rangle$, $|a'\rangle = |a\rangle$ is given in second order by

$$K^{aa}_{bb} = \sum_l \Gamma^p_{l,ba} = \sum_l \frac{\mathrm{i}}{\hbar}\lim_{\lambda\to 0^+}\int \mathrm{d}\epsilon\, \frac{\gamma_l^{ba}(\epsilon) f_l^p(\epsilon)}{E_a^b - \epsilon + \mathrm{i}\,\lambda} + \mathrm{H.c.},$$

where $\Gamma^p_{l,ba}$ is the corresponding tunneling rate. The function $f_l^p(\epsilon)$ with $p = \pm$ is defined as $f_l^\pm(\epsilon) = [1 + \exp\{\pm\beta(\epsilon - \mu_l)\}]^{-1}$, where β is the inverse temperature and μ_l the lead's chemical potential. Hence, $f_l^+(\epsilon) = f_l(\epsilon)$ is the Fermi function and describes the occupation probability in lead l. In general, $p = \pm 1$ if the final state $|b\rangle$ has one electron more/less than the initial state $|a\rangle$. The energy difference between final and initial dot configuration is given by $E_a^b = E_b - E_a = \tilde{E}_b - \tilde{E}_a - e\alpha V_\mathrm{g}(N_b - N_a)$. Finally,

$$\gamma_l^{ba}(\epsilon) = \gamma_{l\sigma(b,a)}(\epsilon) = |T_l|^2\mathcal{D}_{l\sigma}(\epsilon)$$

is a spin-dependent linewidth defined in terms of the tunneling amplitude T_l and of the spin-dependent density of states $\mathcal{D}_{l\sigma}(\epsilon)$. A Lorentzian provides a cutoff for the density of states at a bandwidth W. The notation $\sigma(a,b)$ indicates that the spin σ of the electron tunneling out of/onto lead l depends on the spin configuration of the initial state a and the final state b of the quantum dot. It is convenient to introduce the spin-resolved density of states of lead l at the Fermi energy

$$\mathcal{D}_{l\sigma} = \mathcal{D}_{l\sigma}(\epsilon_\mathrm{F}) = D_0(1 + \sigma P_l)/2, \quad (4)$$

where $P_l = (\mathcal{D}_{l\uparrow} - \mathcal{D}_{l\downarrow})/(\mathcal{D}_{l\uparrow} + \mathcal{D}_{l\downarrow})$ is the polarization of lead l. The couplings $|T_l|^2$ we define in the same spirit as

$$|T_{s/d}|^2 = |T_0|^2(1 \pm a)/2, \quad (5)$$

using the parameter a to tune the asymmetry in the coupling to the leads. We will in the following use the factorization

$$\gamma_{l\sigma(b,a)}(\epsilon_\mathrm{F}) = \gamma_0\kappa_{l\sigma}, \quad (6)$$

where we collect the lead and spin independent prefactors in an overall coupling strength $\gamma_0 = D_0|T_0|^2$ and include the dependence on spin and lead index in the dimensionless parameter $\kappa_{l\sigma}$, where $\sum_{l\tau\sigma}\kappa_{l\sigma} = 1$. Note that γ_0 is related to the level broadening Γ_0 by $\Gamma_0 = 2\pi\gamma_0$.

In Fig. 6(a), a diagrammatic representation of one contribution to the second order kernel is shown for the case of $|a\rangle = |0\rangle$ and $|b\rangle = |\tau\sigma\rangle$. The fermionic line connecting the lower to the upper contour carries indices l,ϵ,σ which fully characterize the nature of the electron tunneling between lead l and quantum dot. The direction of the arrow further specifies if the electron tunnels out of (towards lower contour) or onto (towards upper contour) the dot. Beside this lowest (second) order contribution, we consider all diagrams of the structure shown in Fig. 6(b). The selected diagrams contain arbitrary

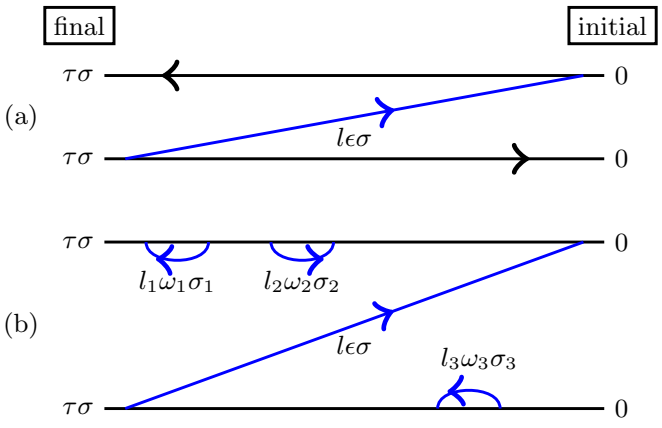

FIG. 6. (Color online) Diagrammatic representations of the contributions to the rate $\Gamma^+_{l,\tau\sigma 0}$ in second order (a), and an example of diagrams included in the DSO (b). In the latter case, the fermion line (blue) from the second-order theory is "dressed" by charge fluctuation processes. The labels below the fermion lines denote energy and spin of the particle tunneling from/onto the lead. Note that the diagram is read from right to left, i.e., the initial state $|0\rangle$ can be found on the right and the final state $|\tau\sigma\rangle$ on the left.

numbers of uncorrelated charge fluctuation processes (bubbles in Fig. 6). During the charge fluctuation, the dot state on the upper contour has one charge less or more compared to that of the final state $|\tau\sigma\rangle$. Hence the virtual state is either the state $|0\rangle$ or one of the many (see Table I) doubly occupied states. On the lower contour, the fluctuations take place with respect to the initial state $|0\rangle$. Examples of charge fluctuations in the case of initial state $|0\rangle$ and final state $|K\uparrow\rangle$ are shown in Fig. 7. Summing all diagrams of this type yields the DSO rates:

$$\Gamma^+_{l,ba} = \frac{1}{2\pi\hbar}\int \mathrm{d}\epsilon\; \nu_l^{ba}(\epsilon) f_l^+(\epsilon), \quad (7)$$

for a state b that can be reached by an in-tunneling process from state a, and

$$\Gamma^-_{l,ab} = \frac{1}{2\pi\hbar}\int \mathrm{d}\epsilon\; \nu_l^{ba}(\epsilon) f_l^-(\epsilon) \quad (8)$$

for an out-tunneling process $b \to a$. Note that we introduced a tunneling-like density of states (TDOS)

$$\nu_l^{ba}(\epsilon) = \frac{\gamma_l^{ba}(\epsilon)\,\mathrm{Im}\,(\Sigma^{ba}(\epsilon))}{\left[\mathrm{Im}\,(\Sigma^{ba}(\epsilon))\right]^2 + \left[\epsilon - E_a^b + \mathrm{Re}\,(\Sigma^{ba}(\epsilon))\right]^2}. \quad (9)$$

We refer to the contribution Σ^{ba} in the denominator of the TDOS as a self-energy that infers from the contributions of all possible charge fluctuations connected to the initial, a, and final, b, states in the state space given in Table I. Explicitly,

$$\Sigma^{ba}(\epsilon) = \sum_{\substack{c\,\in\,\{b,a\}\\ c'\,\in\,C_c^\pm}} a_{ba}^{c'c}(\epsilon), \quad (10)$$

with the sets $C^\pm_{b/a}$ given by

$$C^\pm_{b/a} := \{c' : N_{c'} = N_{b/a} \pm 1 \wedge 4n - 1 \leqslant N_{c'} \leqslant 4n + 5\}. \quad (11)$$

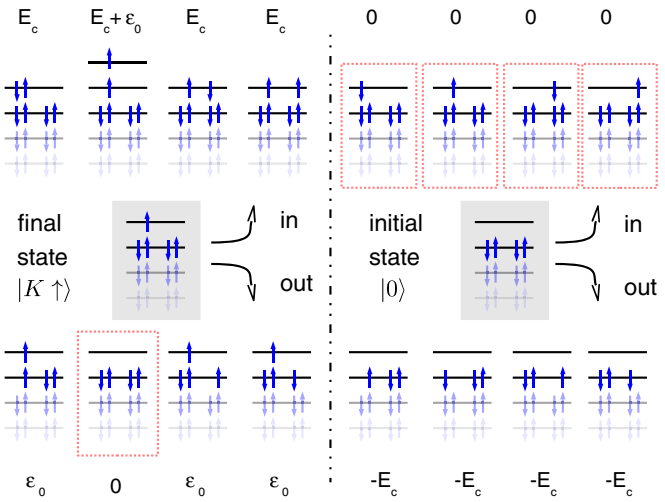

FIG. 7. (Color online) Example of possible charge fluctuations for a final state ($|K\uparrow\rangle$, left, shaded gray) with one extra electron and an initial state with zero electrons in the shell n ($|0\rangle$, right, shaded gray). This set corresponds to one specific diagram of the type shown in Fig. 6(b). States that can be reached by in-tunneling of an electron are shown on top, states that can be reached by out-tunneling of an electron are shown on the bottom. Dashed frames highlight resonant ($E^{c'/b}_{a/c'} = 0$) charge fluctuations. Above and below the level schemes, the energy difference between the virtual state and the state on the other contour is given: the energies of the states accessible from the initial (final) state are compared to the energy of the final (initial) state on resonance ($\tilde{E}^{K\uparrow}_0 = e\alpha V_g$). Note that the electron number of the states that can be reached by in-tunneling on the left and the number of electrons in the initial state on the right differ by two. The same situation occurs for the final state and the out-tunneling states on the right. The energy differences for this class of fluctuations is of the order of E_c. A comparison of the electron number of the final state with the in-tunneling states on the left and the initial state with the out-tunneling states on the right yields a difference of zero. These fluctuations have comparably low energy cost.

The sets are shown in Fig. 7 for the states $|a\rangle = |0\rangle$ and $|b\rangle = |K\uparrow\rangle$. The summand

$$a^{c'(b/a)}_{ba}(\epsilon) = \sum_l \int \mathrm{d}\omega \, \frac{\gamma_l^{c'(b/a)}(\omega) f_l^p(\omega)}{\pm p\omega + \epsilon - E^{c'/b}_{a/c'} + \mathrm{i}\,\eta}$$

accounts for a transition from b or a to a state c', with $c' \in C^p_{b/a}$. Performing the integral, we arrive at an analytic expression for the contributions to the self-energy, i.e.,

$$\begin{aligned} a^{c'(b/a)}_{ba}(\epsilon) &= \sum_l \gamma_l^{c'(b/a)}(\epsilon)\big[\mathrm{i}\,\pi f_l^p\big(\pm p\big(E^{c'/b}_{a/c'} - \epsilon\big)\big) \\ &\quad \pm \big(\hat{\Psi}^{(0)}(W) - \mathrm{Re}\big\{\hat{\Psi}^{(0)}\big[\mathrm{i}\,\big(\mu_l \pm p\big(E^{c'/b}_{a/c'} - \epsilon\big)\big)\big]\big\}\big)\big], \end{aligned} \tag{12}$$

where $\hat{\Psi}^{(0)}(x) = \Psi^{(0)}(0.5 + x/2\pi k_B T)$ and $\Psi^{(0)}$ is the digamma function. Note that the dependency on the bandwidth drops out due to the alternating sign of the contributions from the upper and lower contour in the summation in Eq. (10). Having calculated the self-energy, we are now able to collect all rates according to the transitions in our state space, and solve the stationary Eq. (3) to obtain the occupation probabilities $\rho_{aa} = P_a$. Within the steady state limit, we can neglect off-diagonal entries ρ_{ba} if they are among nondegenerate states [21]. According to Table I, the CNT spectrum can be spin and valley degenerate. However, the tunneling Hamiltonian (2) conserves the spin during tunneling, and thus spin coherences are not present in the dynamics. Here, for simplicity, orbital coherences are neglected as well.[1]

C. Current within the DSO

The current through the terminal l can be written in terms of the difference of in- and out-tunneling contributions at the junction [37]:

$$I_l(\mathrm{V_b}) = \frac{e}{2\pi\hbar} \sum_{\substack{a\in C \\ c\in C_a^+}} \int \mathrm{d}\epsilon \times \big[P_a(\mathrm{V_b}) f_l^+(\epsilon) - P_c(\mathrm{V_b}) f_l^-(\epsilon)\big] \nu_l^{ca}(\epsilon, \mathrm{V_b}), \tag{13}$$

where $\mathrm{V_b}$ is the bias voltage applied between the two contacts, and C is the set of all possible configurations (see Table I). In general, the populations can be expressed in terms of rates via the Liouville equation (3) and a closed form for the current and, consequently, for the conductance can be found. This is straightforward if two states are connected by pairwise gain-loss relations [37]. For the case of the single-impurity Anderson model, for example, a compact notation of the conductance can be given [22].

The width of a resonance in conductance with respect to the gate potential is determined by the populations, the TDOS which has a form similar to a Lorentzian, and by the derivative of the Fermi functions. Note that the populations are themselves a function of the rates and therefore are also governed by the resonance conditions of the rates. The DSO theory has been proven to be quantitatively valid down to temperatures $4k_BT \sim \gamma_0$ in the single electron transistor [22]. Upon decreasing of the temperature below $\gamma_0/4$, a quantitative description of the transition rate Γ_l^{ac} would require to calculate Σ beyond the lowest order in γ_0. In the regime where temperature and coupling are of comparable magnitude, the width and position of the Coulomb blockade peaks in a gate trace are strongly influenced by the TDOS and, more precisely, by the self-energy Σ. The role of $\mathrm{Re}(\Sigma)$ is to influence the positions of the Coulomb blockade peaks: In the rate for the transition a to b, the real part appears next to the energy difference E_a^b of the transition in the denominator. Hence, due to this contribution the resonant level is shifted depending on the configuration of the leads.

[1]For CNTs of the zigzag type, coherences are not expected to contribute to the dynamics for tunneling processes which conserve the crystal angular momentum, i.e., for which the perpendicular component $k_\perp$ of the momentum $\mathbf{k}$ is conserved during tunneling. This is because in zigzag type CNTs the two valleys correspond to different values of the crystal angular momentum.

D. Renormalization of excited states

In the stability diagram in Fig. 2 we observe an asymmetry in the spacing of lines associated with excited states connected to one charging state, as drawn schematically in Fig. 8. The line $0 \rightarrow 1'$ meets the diamond at bias voltage V_{b1}. Measured along the bias voltage axis, this value is larger than the energy difference V_{b2} associated with the line $2 \rightarrow 1'$ on the right. A similar behavior has been discussed previously for the co-tunneling regime [32]. As noted by these authors, the asymmetry can not be explained within the sequential tunneling picture but can be attributed to the renormalization of the excitation energies E_a^b in Eq. (9) due to virtual tunneling processes. Although the framework in Ref. [32] is different, the evaluation of $\mathrm{Re}(\Sigma^{ba})$ is similar to that in our model. The condition for a resonance for a transition between states a and b is given by

$$\epsilon \pm e\,\mathrm{V_b}/2 + e\alpha V_g - \tilde{E}_a^b + \mathrm{Re}(\Sigma^{ba}) = 0, \qquad (14)$$

where ϵ is the energy of the tunneling electron with respect to the chemical potential of the unbiased contact μ_0. Note that this condition can be fulfilled for different transitions at the same time, a situation that occurs at any point where two lines in a stability diagram intersect. In order to interpret the observed shift of the excited state line in the differential conductance data in Fig. 7, it is illuminating to study the contribution from $\mathrm{Re}(\Sigma)$ at points (V_{g1}, V_{b1}) and (V_{g2}, V_{b2}) marked by a dot and a circle, respectively, in Fig. 8. We consider an exemplary set of states $0 = |0;n\rangle$, $1 = |K\uparrow;n\rangle$, $1'_1 = |[K\uparrow];n\rangle$, $1'_2 = |K\uparrow,K\downarrow,(K'\uparrow);n\rangle$ and $2 = |K\uparrow,K\downarrow;n\rangle$. A similar analysis can be carried out for other states with $4n+1$ and $4n+2$ electrons. The quantum numbers in round brackets denote a missing electron of shell $n-1$ whereas the square brackets indicate a state of shell $n+1$. For each of the highlighted points in Fig. 8, two conditions in the form of Eq. (14) can be given. Subtracting them pairwise, we are left with

$$eV_{b1} - E_1^{1'} + [\mathrm{Re}(\Sigma^{1',0}) - \mathrm{Re}(\Sigma^{1,0})] = 0, \qquad (15)$$

$$eV_{b2} - E_1^{1'} + [\mathrm{Re}(\Sigma^{2,1}) - \mathrm{Re}(\Sigma^{2,1'})] = 0, \qquad (16)$$

where the self-energy contributions depend on bias and gate voltage. To lowest order in γ_0, we analyze the differences in $\mathrm{Re}(\Sigma)$ using $eV_{b1/2} = E_1^{1'}$ and $\alpha e V_g^{1/2} = \tilde{E}_{0/1}^{1/2} \pm eV_b/2$ at $\epsilon = 0$. In order to calculate $\mathrm{Re}(\Sigma)$, we have to analyze the contributions from all accessible states in Eq. (10). In principle, there are arbitrarily many states that can be reached by a charge fluctuation. However, we assert that the available energy interval for charge fluctuation processes is given by $\max(eV_b, \Gamma_0, 3-4k_BT)$ and contributions beyond this scale are suppressed. Numerical results using a larger bandwidth can be found in Appendix A.

For our considerations, we assume that the spin orbit coupling of our CNT quantum dot is small, i.e., $\Delta_{SO} < \max(k_BT, \Gamma)$. Otherwise, we would expect to see a twofold symmetry in the spacing of the excited state lines in the stability diagram in Fig. 2. The other important scales—charging energy, shell spacing and linewidth—are related in the way $E_c > \epsilon_0 \gg \max(k_BT, \gamma_0)$. Within this choice of parameters the difference of the self-energy corrections for the resonant transition can be calculated by (15)−(16)= 0, i.e.,

$$\begin{aligned}\delta_1 &\equiv [\mathrm{Re}(\Sigma^{1'0}) - \mathrm{Re}(\Sigma^{10})] - [\mathrm{Re}(\Sigma^{21}) - \mathrm{Re}(\Sigma^{21'})] \\ &\simeq \gamma_0\{-1 + 2\bar{\kappa}_s - \bar{\kappa}_d + \bar{\kappa}_\uparrow - \bar{\kappa}_\downarrow\}\Psi_R^0(\epsilon_0/2), \qquad (17)\end{aligned}$$

where we used the abbreviation $\Psi_R^0(\epsilon) = \mathrm{Re}[\Psi^0(1/2 + i\epsilon/2\pi k_BT)]$ and a bar denotes a summation over indices, e.g., $\bar{\kappa}_l = \sum_\sigma \kappa_{l\sigma}$. A detailed derivation of these quantities is given in Appendix B. Similar calculations are performed for the excited states in the $n+2$ and $n+3$ diamonds, yielding

$$\begin{aligned}\delta_2 &\simeq \gamma_0\{\bar{\kappa}_s - \bar{\kappa}_d + \kappa_{s\downarrow} - \kappa_{d\uparrow}\}\Psi_R^0(\epsilon_0/2), \\ \delta_3 &\simeq \gamma_0\{1 + \bar{\kappa}_s - 2\bar{\kappa}_d + \bar{\kappa}_\downarrow - \bar{\kappa}_\uparrow\}\Psi_R^0(\epsilon_0/2),\end{aligned}$$

where the states with three electrons are chosen to be electron-hole symmetric with respect to the state with one electron. Note that for the case of symmetric couplings the shifts reflect the electron-hole symmetry of the system while a choice of $a \neq 0$ [Eq. (5)] breaks this symmetry. For highly asymmetric couplings $|a| \sim 1$, the shifts are comparable to those in Ref. [32]. Note that the effective change of the resonance with respect to the energy difference has a negative sign [compare Eq. (14)]. The resonance marked by the left arrow in Fig. 2 is situated above the resonance marked by the right arrow. The experimental data thus corresponds to a negative shift. We therefore assume an asymmetric coupling to the leads with a dominant coupling to the drain contact, i.e., $\kappa_s < \kappa_d$, $-1 < a < 0$. Using the parameters from a fit to the data in Sec. V, i.e., $a = -0.7$ and $\epsilon_0 = 1.4$ meV, we obtain $\delta_1 \approx -0.2$ meV and $\delta_2 \approx -0.1$ meV. Compared to the shifts in the experimental data, these values are too small by a factor of 2–3. We expect that additional states may contribute to the charge fluctuations that are not considered within this approximation.

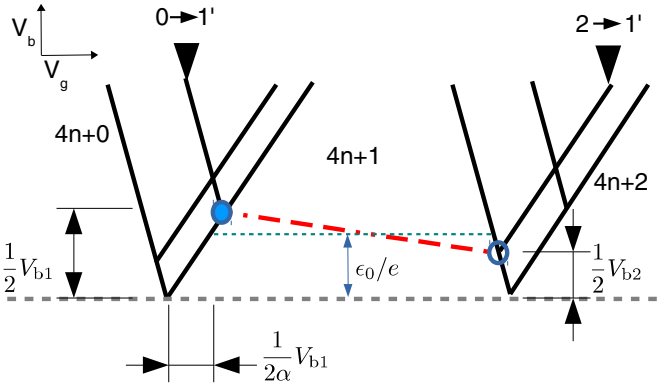

FIG. 8. (Color online) Schematic drawing of the conductance lines in the vicinity of the charging state with $4n+1$ electrons in Fig. 2. The first visible excitation is shifted upwards on the left and downwards on the right side of one charging diamond by $e(V_{b1} - V_{b2})/2 = -\delta_1$. The corresponding energies in Fig. 2 are $eV_{b1}/2 \simeq 2$ meV and $eV_{b2}/2 \simeq 1.4$ meV. For our analysis, we choose bias and gate voltages close to the filled dot for the first transition $0 \rightarrow 1'$ and to the empty circle for the second transition $2 \rightarrow 1'$.

E. Tunneling magnetoresistance

Corrections to the conductance peak width are given by $\mathrm{Im}(\Sigma)$. Because $\mathrm{Re}(\Sigma)$ and $\mathrm{Im}(\Sigma)$ both depend on the different magnetic properties of the source and drain leads as well as on the dot's configuration, the resulting impact on the TMR is quite intricate. Thus we analyze the contributions to the self-energy in the light of different configuration of the lead's polarizations. We focus on the last resonance, i.e., the transitions $|0,n+1\rangle \rightleftarrows \{|(\sigma\tau),n+1\rangle\}$ where the TMR graph in Fig. 4 exhibits a double dip like structure. The back-gate voltage is tuned such that

$$\epsilon + e\alpha V_\mathrm{g} - \tilde{E}^0_{(\tau\sigma)} + \mathrm{Re}(\Sigma^{0,(\tau\sigma)}) = 0,$$

and the quantum numbers in round brackets $(\tau\sigma)$ denote a missing electron of shell $n+1$. At lowest order in the tunnel coupling γ_0, we approximate $e\alpha V_\mathrm{g} = \tilde{E}^0_{(\tau\sigma)}$ when we calculate $\mathrm{Re}(\Sigma^{0,(\tau\sigma)})$. From Eq. (12), we list the imaginary part of the self-energy for this transition, i.e.,

$$\begin{aligned}\mathrm{Im}(\Sigma^{0,(\tau\sigma)}) = \pi\gamma_0 \sum_l \Bigg[&\sum_{c\in C_0^+} \kappa_{l\sigma(c)} f_l^+\big(E^c_{(\tau\sigma)} - \epsilon\big) \\ &+ \sum_{c'\in C_0^-} \kappa_{l\sigma(c')} f_l^-\big(\epsilon - E^{c'}_{(\tau\sigma)}\big) \\ &+ \sum_{c\in C^+_{(\tau\sigma)}} \kappa_{l\sigma(c)} f_l^+\big(\epsilon - E^0_c\big) \\ &+ \sum_{c'\in C^-_{(\tau\sigma)}} \kappa_{l\sigma(c')} f_l^-\big(E^0_{c'} - \epsilon\big) \Bigg].\end{aligned}$$

The magnitude of the energy difference of the virtual state with respect to the state on the other contour determines whether a possible charge fluctuation contributes to the renormalization of the self-energy or not: a contribution $f_l^+(E_\mathrm{c} - \epsilon)$, e.g., is exponentially suppressed in the vicinity of the resonance.

Therefore, knowing the arguments in the step functions $f^\pm$, we can simplify the result significantly. Close to the resonance where $|\epsilon| < \max(k_B T, \gamma_0)$, the fluctuations with an energy cost of the charging energy E_c or of the shell spacing ϵ_0, e.g., the states that can be reached by out-tunneling from the state $|(\tau\sigma)\rangle$ can be neglected. Focusing on the resonant contributions, we are left with

$$\frac{\mathrm{Im}(\Sigma^{0,(\tau\sigma)})}{\pi\gamma_0} \simeq \sum_l \left[\kappa_{l\sigma} f_l^+(\epsilon) + \sum_{\tau'\sigma'} \kappa_{l\sigma'} f_l^-\big(\epsilon - E^{(\sigma')}_{(\sigma)}\big) \right]. \tag{18}$$

It is clear from this result that the broadening of the TDOS peak does depend on the lead configuration $\{\kappa_{l\sigma}\}$. Let the majority spins be polarized such that $\sigma = +1$ in the layout with parallel lead polarization. The sum over the leads is then given by $\sum_l \kappa^\mathrm{p}_{l\sigma} = (1+\sigma P)/4$ and $\sum_l \kappa^\mathrm{ap}_{l\sigma} = (1+\sigma Pa)/4$ for parallel and antiparallel polarizations, respectively. Let us first consider the case of zero effective Zeeman splitting, i.e., $E^\sigma_{\bar{\sigma}} = E^{(\bar{\sigma})}_{(\sigma)} = 0$. The difference of $\mathrm{Im}(\Sigma)$ for the two configurations then reads

$$\mathrm{Im}\left[\Sigma^{0,(\tau\sigma)}_\mathrm{p} - \Sigma^{0,(\tau\sigma)}_\mathrm{ap}\right] = \delta^\mathrm{Im} = \pi\tfrac{\gamma_0}{4}\sigma P(1-a) f^+(\epsilon). \tag{19}$$

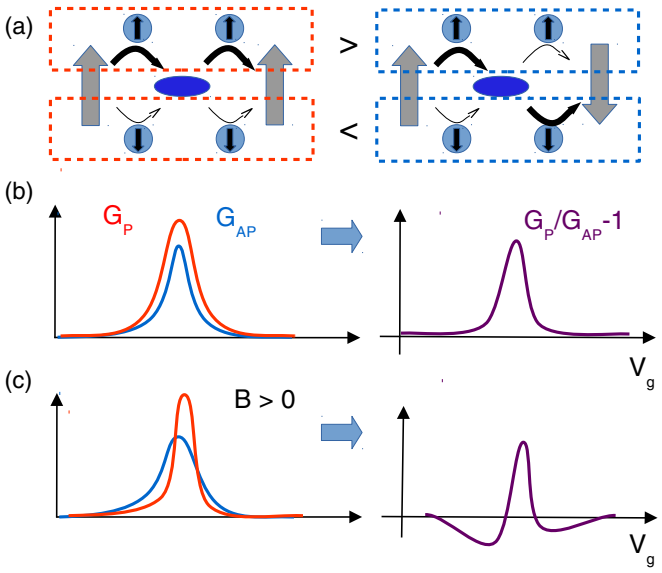

FIG. 9. (Color online) The influence of $\mathrm{Im}(\Sigma)$ on the TMR. (a) Large gray arrows symbolize the majority spin in the left or right contact. The contributions to the self-energy for one spin species are summed for each configuration of polarized leads (parallel on the left, antiparallel on the right) as indicated by the dashed frames. Weak (strong) coupling to the dot (blue ellipse) is given by thin (thick) arrows. Note that for the spin-down species the sum over the leads yields a greater contribution in the configuration with antiparallel polarization (as indicated by the signs between the dashed frames). (b) On the left, we depict schematically the conductance peaks for one resonance in both parallel and antiparallel configurations and the resulting TMR (right). The broadening of G_p is typically larger than for G_ap in the absence of stray fields. (c) Due to a magnetic stray field, the contribution to $\mathrm{Im}(\Sigma)$ in the parallel case can be reduced, giving rise to a double dip structure in the TMR.

Note that the validity of this result depends on the ratio of linewidth and level spacing, namely that $\gamma_0 \ll \epsilon_0$ such that only the selected small set of charge fluctuations contribute. The sign of the difference in Eq. (19) is determined by σ, a result which is intuitively clear since the sum over the couplings will be greater for the spin-up transition ($\sigma = 1$) in the parallel case and for the spin-down transition in the antiparallel one ($\sigma = -1$), as shown schematically in Fig. 9(a). For zero energy splitting $E^{(\bar{\sigma})}_{(\sigma)}$, we would expect a broadening of the peak associated with the transition $0 \rightleftarrows (\uparrow)$ for the parallel configuration and a broadening of the peak in G^ap for the transition $0 \rightleftarrows (\downarrow)$. Note, however, that the second effect will not be visible since the TMR ratio will be dominated by the spin up transition. Hence, we will observe a TMR signal as depicted in Fig. 9(b).

Now let us assume a nonzero effective Zeeman splitting $E^\uparrow_\downarrow = E_\uparrow - E_\downarrow = g\,\mu_\mathrm{B}\,h_\mathrm{p/ap}$ of states with quantum numbers $\sigma = \uparrow / \downarrow$. This splitting also depends on the magnetization state p (parallel) or ap (antiparallel) of the contact electrodes. The energy difference is expressed in terms of the effective magnetic fields $g\mu_\mathrm{B}h_\mathrm{p}$ and $g\mu_\mathrm{B}h_\mathrm{ap}$. We assume that this field is nonzero for both polarizations. $\mathrm{Im}(\Sigma)$ as well as the TMR are very sensitive to the choice of the shifts, the couplings and the polarization. The mechanism we want to discuss can be

observed for different parameter regimes, but for the sake of the argument it is sufficient to present one possible set that we deduce from the experiment and the line of reasoning that goes with it. In the last part of Sec. III D, we argue that couplings $\kappa_s < \kappa_d$, or, similarly, $0 > a > -1$ are needed to explain the shift of the excited state lines in Fig. 2. Furthermore we point out that the peaks in conductance in Fig. 4 are descending in height as we fill the shell. In our model, the drain lead switches polarization upon interaction with external magnetic field, while the density of states in the weakly coupled source contact remains unaltered. Given that the spin transport is more sensitive to the bottleneck (source) contact, it is plausible to assume that the shifts are such that the majority spins tunnel first on the quantum dot, namely spin up electrons in both configurations. These considerations favor a choice of negative shifts $g\mu_B h_{ap}, g\mu_B h_p < -k_B T$. The second pair of resonances is then dominated by spin down electrons and the respective contributions $f^-(\epsilon + g\,\mu_B\,h_{p/ap})$ in Eq. (18) are suppressed. Conversely, for spin-up electrons $f^-(\epsilon - g\,\mu_B\,h_{p/ap}) = 1$. In the resonant case, $|\epsilon| \lesssim k_B T$, the imaginary part of the self-energy for the $|0\rangle \leftrightarrows |(\sigma)\rangle$ then reads

$$\delta^{\mathrm{Im}} \simeq -\pi \frac{\gamma_0}{4}(1-a)P[1-\sigma f^-(\epsilon)]. \tag{20}$$

The magnitude of the relative broadening of the peak related to the transition of a spin down electron in G_{ap} is thus increased for higher polarization and $a \to -1$. Although this estimate is only valid in the direct vicinity of the resonance, it describes the situation qualitatively as can be seen in Fig. 10. We show conductance and TMR nearby the resonance $|0,n+1\rangle \rightleftarrows \{|(\sigma\tau),n+1\rangle\}$ for fields $g\mu_B h_p = -40\ \mu$eV and $g\mu_B h_{ap} = -80\ \mu$eV. In the panels on the left side, the polarization is varied keeping $a = -0.8$ fixed. We see that the right shoulder in the TMR curve (c) is lifted upwards with increasing polarization. On the right panels in Fig. 10, we increase the coupling to the source contact which is proportional to a. While the conductance is decreased for asymmetric choices of a in both configurations [see (d) and (e)], the magnitude of the peak in G_{ap} is not symmetric with respect to the coupling to source and drain. The TMR in Fig. 10(c) can be related to Eq. (20): the shoulders for $a = 0.8$ turn into dips approaching $a = -0.8$. Please keep in mind that this discussion is simplified since we do not account for the fact that the relative position of the peaks changes, too, as we vary the parameters a and P [compare Re(Σ) and Im(Σ) plotted in Fig. 12 in Appendix A].

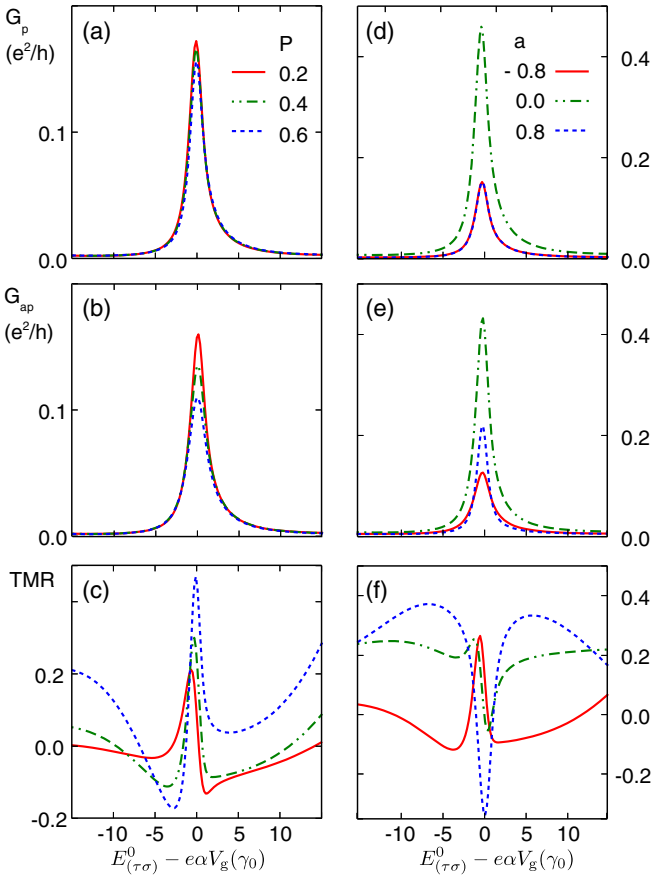

FIG. 10. (Color online) Conductance and TMR calculations in the vicinity of the resonance $|0,n+1\rangle \rightleftarrows \{|(\sigma\tau),n+1\rangle\}$ for different polarizations P [(a)–(c), $a = -0.8$] and coupling asymmetry a [(d)–(f), $P = 0.4$] applied in the parallel configuration for effective Zeeman splitting $g\mu_B h_p = -40\ \mu$eV and $g\mu_B h_{ap} = -80\ \mu$eV. (a) and (b) Increasing the polarization reduces the peak width and height of both G_p and G_{ap}. (c) In the TMR curve, the shoulder on the left at $P = 0.2$ is shifted to the right for $P = 0.6$. (d) and (e) The coupling asymmetry $a \neq 0$ diminishes the peak heights of the conductance for both configurations of the leads. Note that in the antiparallel case shown in (e) the symmetry between the contacts is broken and the peak height is sensitive to the variation of the dominating coupling. (f) The TMR curve exhibits a double dip feature for values $-1 \lesssim a < 0$. It is transformed to a double peak for $0 < a \lesssim 1$. All plots are calculated at a temperature corresponding to 40 μeV and a coupling $\gamma_0 = 160\ \mu$eV.

IV. COMPARISON

A. Conductance in the experiment and in the model

In Fig. 11(a) (blue circles), we show the conductance G_p^{fast} obtained at $B = 0$ performing a *fast* measurement, i.e., sweeping the gate voltage V_g at zero bias voltage, see Sec. II B. Note that it provides only conductance data for the parallel configuration (compare Fig. 3). The data from this measurement yields conductance peaks that fit to Lorentzian curves with an average FWHM of 0.3 meV. Adapting our model parameters to the data of G_p^{fast}, we obtain the continuous lines in Figs. 11(a), 11(b), and 11(d). The conductance data from the *slow* measurement (compare Sec. II B) for the two configurations, G_p^{slow} and G_{ap}^{slow}, are shown in Figs. 11(a) and 11(b) (green crosses). The shape of the conductance peaks turns out to be non-Lorentzian, with the peak height in the conductance data limited to $\sim$0.1 e^2/h. While the flanks of the peaks match for the first three resonances in the data from the slow and from the fast measurement,[2] the maximum conductance values deviate by a factor of three. So far, no full explanation for the suppression of the peak conductance was found.

[2]There is a deviation between G_p^{fast} and G_p^{fast} in Fig. 11(a) at the right flank of the second resonance at $V_g = 8.15$ V due to jump in the gate voltage during the measurement.

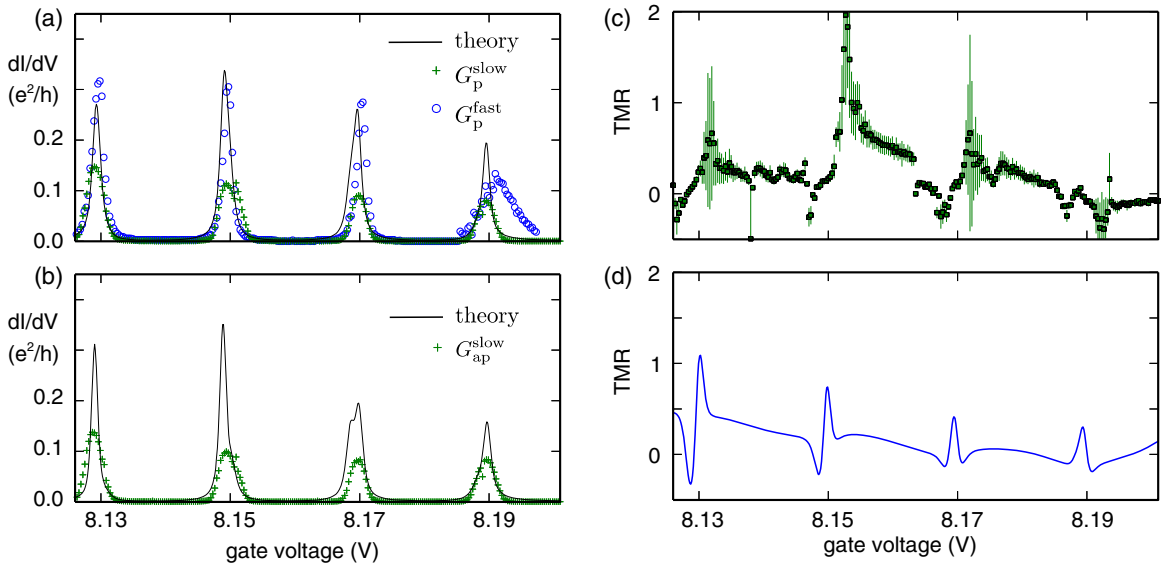

FIG. 11. (Color online) Conductance at zero bias as a function of gate voltage V_g plotted for (a) parallel and (b) antiparallel polarization of the leads. In (a), a gate trace [$G_p^{fast}(V_g)$, blue circles] is shown together with conductance obtained during TMR measurements $G_p^{slow}(B,V_g)$ (green crosses, see also Fig. 4), and the calculated conductance for parallel lead polarization (continuous line, black) at $k_BT = 40$ μeV, $\epsilon_0 = 1.4$ meV, $E_c = 6.1$ meV, $a = -0.7$, $P = 0.4$, $g\mu_B h_{ap} = -0.16$ meV, and $g\mu_B h_p = -0.12$ meV. In the vicinity of the rightmost resonance, G_p^{fast} shows a high noise level (compare also Fig. 2). (b) The conductance data measured for antiparallel polarization of the contacts $G_{ap}^{slow}(B,V_g)$ (green crosses) is compared to the model output (continuous line, black) for the same parameters as in (a). (c) Experimental TMR data calculated from G_p^{slow}(a) and G_{ap}^{slow}(b) (also shown in Fig. 4). (d) TMR obtained from the model conductance [continuous lines in (a) and (b)].

B. Model parameters

A bare coupling of $\gamma_0 = 80$ μeV is found to optimize the fit to G_p^{fast}. The thermal energy is chosen as $k_BT = 40$ μeV (460 mK), close to the base temperature (300 mK). For the quantum dot parameters we set $E_c = 6.1$ meV and a shell spacing $\epsilon_0 = 1.4$ meV as inferred from Sec. II. The shell number $n \sim 40$ is estimated from the distance to the band gap. We assume asymmetric contacts with $a = -0.7$ and polarization $P = 0.4$. For the calculation of the charge fluctuations, we include all states within an energy interval of $3\epsilon_0$ (see Appendix A). The effective Zeeman shifts for the model output in Fig. 11 are $g\mu_B h_p = -0.12$ meV and $g\mu_B h_{ap} = -0.16$ meV.

C. Discussion

If only features of the leads density of states at the Fermi energy are included, compare Eq. (4), the DSO preserves particle-hole symmetry by construction [22]. To break this symmetry, a Stoner-shift of the majority band with respect to the minority band should be included [25], whose effect is analogous to that of an effective Zeeman field [21]. Such effective fields have also been used to model the effects of coherent reflections at the magnetic interfaces in double barrier systems [7]. Since the data in Figs. 11(a)–11(c) does not reflect particle hole symmetry, we use effective Zeeman splittings to break the particle-hole symmetry and reproduce the observed magnitude of the TMR effect. The splittings are of similar magnitude as those used in Ref. [20] ($g\mu_B h_p = 0.25$ meV and $g\mu_B h_{ap} = 0.05$ meV) to explain the experimental TMR data of Ref. [7].

In case of nonzero spin-orbit coupling [38,39], we would expect a splitting of the excited state lines in the stability diagram in Fig. 2. This is not resolved in our experimental data. For simplicity we therefore here assume $\Delta_{SO} = 0$. Model calculations with nonzero spin orbit coupling can be found in Appendix C.

From the conductance traces calculated within our model, Figs. 11(a) and 11(b) (continuous lines), the TMR, Fig. 11(d), is obtained. The data and the model calculation agree in the decay of the TMR amplitude within a sequence of four charging states including the "double dip" feature in the last two resonances at $V_g = 8.17$ and 8.19 V. This indicates that the sequence in Fig. 11 represents one shell, i.e., charging states $4n + 1$ to $4(n + 1)$. We note that in the model output the last resonance is dominated by a peak while the dips are more prominent in the experimental data.

In the vicinity of all conductance peaks (at $V_g = 8.13$, 8.15, 8.17, and 8.19 V), an additional small shoulder around TMR = 0 occurs in the data of Fig. 11(c). These shoulders are likely related to the aforementioned suppression of the peak conductance in the *slow* measurement [see Figs. 11(a) and 11(b)]. We recall that the TMR is calculated from the ratio G_p/G_{ap} (compare also Figs. 5 and 9): in the regions where the peaks are cut off, the ratio G_p^{slow}/G_{ap}^{slow} is smaller than it is in the same region in the model output, where steep peak flanks lead to a larger ratio G_p/G_{ap}.

V. SUMMARY

The tunneling magnetoresistance of a carbon-nanotube based quantum dot with ferromagnetic leads has been explored both experimentally and theoretically. The experimental data

shows a distinct variation of the tunneling magnetoresistance (TMR) lineshapes within a single quadruplet of charging states.

To model the data, we apply the dressed second-order (DSO) framework based on the reduced density matrix formalism. This theory accounts for charge fluctuations between the quantum dot and the ferromagnetic contacts. Thereby, it goes beyond the sequential tunneling approximation, which can only account for a positive and gate-independent TMR. When the charge fluctuation processes are summed to all orders in the coupling to the leads according to the DSO scheme, they yield tunneling rates where the Lamb shift and the broadening of the resonances are given by the real and imaginary parts of the self-energy, respectively. This is a nontrivial result which yields the tunneling rates for an interacting quantum dot in the intermediate parameter regime $E_c \gg k_B T \sim \Gamma$ depending on the polarization of the contacts.

We explicitly compare the DSO self-energy for different contact magnetizations and show that the DSO modeling can account both for the renormalization of excited states and the specific structures observed in the TMR gate dependence. A comparison of the TMR obtained from the model and from the experimental data shows a qualitative agreement.

ACKNOWLEDGMENTS

We gratefully acknowledge discussions with Johannes Kern, Davide Mantelli, and Daniel Schmid. This work was funded by the Deutsche Forschungsgemeinschaft (DFG) via GRK 1570, SFB 689, and Emmy Noether project Hu 1808-1.

APPENDIX A: CONTRIBUTION OF OTHER EXCITED STATES TO THE RENORMALIZATION OF THE SELF-ENERGY

When we discuss the effect of the charge fluctuations in Secs. III D and III E of the main text, we always focus on the most resonant transitions (see Fig. 7) that are energetically favorable, i.e., on transitions in Eq. (12) with an energy difference $E_{a/c'}^{c'/b}$ of the order of the effective linewidth or below. At zero bias, this is the largest available energy scale in the system. Nevertheless, it is interesting to see how the outcome is affected by increasing the bandwidth and allowing excited states of the neighboring shells to contribute to the charge fluctuation channels. In terms of an effective energy shift in a multilevel quantum dot, the renormalization due to excited states was also discussed in Ref. [21]. To illustrate the effect of such a modification we plot the real and imaginary parts of the self-energy Σ in the vicinity of the transition $|(K\downarrow),n\rangle \rightleftarrows |\cdot,n+1\rangle$ for different sets of charge fluctuations within energy ranges of γ_0, ϵ_0, $2\epsilon_0$, and $3\epsilon_0$ in Fig. 12. We clearly see that the fluctuations from higher shells manifest themselves in additional features in the curves for $\mathrm{Re}(\Sigma)$, Figs. 12(a) and 12(b), and $\mathrm{Im}(\Sigma)$, Figs. 12(c) and 12(d). Note, however, that the zero-bias conductance in our system is only sensitive to a small vicinity of a few $k_B T$ around the resonance. Within this range the high-energy contributions do not change the picture substantially. The analysis of the imaginary part in Sec. III E is thus exact at the level of the self-energy since the

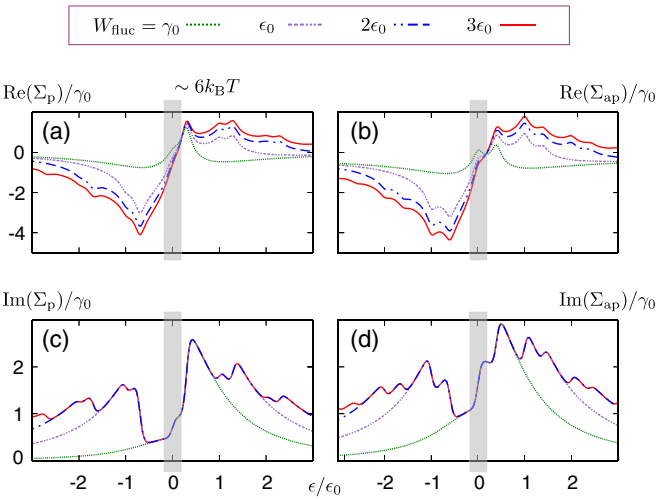

FIG. 12. (Color online) $\mathrm{Re}(\Sigma)$ [(a) and (b)] and $\mathrm{Im}(\Sigma)$ [(c) and (d)] for both lead configurations as a function of energy ϵ in units of the shell spacing ϵ_0. Different lines are plotted for bandwidth $W_{\mathrm{fluc}} = \gamma_0$ (green, dotted) to $3\epsilon_0$ (red, continuous) in steps of ϵ_0. In the vicinity of a few $k_B T$ around the resonance ($\epsilon = 0$, gray region), the difference between the graphs for the real part [(a) and (b)] is small and for the imaginary part [(c) and (d)], it is vanishing.

Fermi functions in the imaginary part suppress contributions from other shells.

APPENDIX B: CALCULATION OF Re(Σ)

In this section, we perform the calculation of $\mathrm{Re}(\Sigma^{1'0}) - \mathrm{Re}(\Sigma^{10})$ as part of the quantity δ_1 introduced in Sec. III D of the main text. To this extent, we analyze the renormalization of the energy difference $E_1^{1'}$ due to charge fluctuations to and from states $0 = |0;n\rangle$, $1 = |K\uparrow;n\rangle$ and $1' = |[K\uparrow];n\rangle$ in more detail. We recall that the real part of the self-energy related to a charge fluctuation to state c' has the form [see. Eq. (12)]

$$-\sum_l \gamma_l^{c'(b/a)}(\epsilon)\Psi_{\mathrm{R}}^0\big(\mu_l \pm p\big(E_{a/c'}^{c'/b} - \epsilon\big)\big),$$

where we have to replace $b = 1'$ and $a = 0$ or $b = 1$ and $a = 0$, respectively. Note that the contribution $\propto \hat{\Psi}^{(0)}(W)$ in Eq. (12) does not appear explicitly since it cancels in the difference of the shifts. Next, we have to find all states c' that contribute within our resonant approximation. We can immediately discard states that can be reached by in-tunneling from b and by out-tunneling from a, since their energy differences $E_{a/c'}^{c'/b}$ are of the order of the charging energy and thus beyond our charge fluctuation bandwidth of $W_e = \max(eV_b, k_B T, \gamma_0) = \epsilon_0/2$. We are left with states that can be reached by in-tunneling into state a and by out-tunneling from state b. Let us discuss one example for the state $1'$. There is one electron in the shell $n+1$ (denoted by the brackets $[\ldots]$ in the state ket) which can tunnel out and we are left with a state $|\cdot,n\rangle$. Actually, this state is identical to the state 0 on the other contour, thus $E_0^{c'=0} = 0$. We can now evaluate the argument of the digamma function, i.e., $\mu_l - E_0^0 + \epsilon$, for $\epsilon = 0$. Since $\mu_{s/d} = \pm\epsilon_0/2$ and thus $|\mu_l| \leqslant W_e$, we have to sum over both leads. The total contribution from fluctuations

to $c' = 0$ is thus $-\gamma_0 \sum_l \kappa_{l\uparrow} \Psi^0_{\rm R}(\epsilon_0/2)$. The other states that can be reached by out-tunneling, e.g., $|(K\uparrow),[K\uparrow],n\rangle$, yield energy differences of at least $3/2\epsilon_0 > W_e$. Using similar arguments, we can collect all relevant contributions to the difference $\mathrm{Re}(\Sigma^{1'0}) - \mathrm{Re}(\Sigma^{10})$. In a graphical representation, this can be visualized as

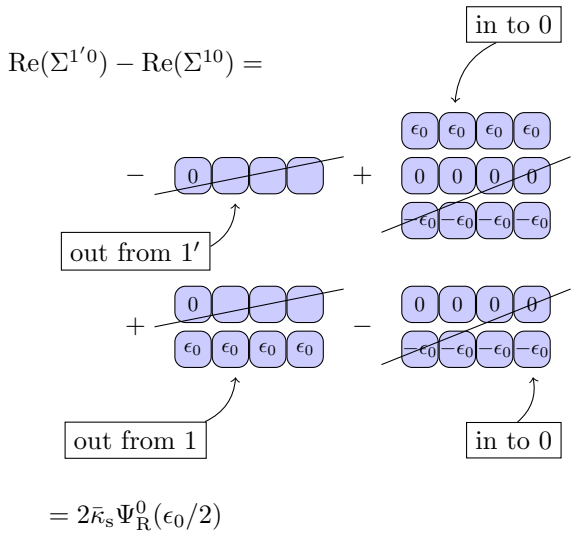

where one set of four boxes symbolizes one shell and we use $E^{c'/b}_{a/c'}$ as a label. Fluctuations that cancel are crossed out. Note that for excited states with an energy difference $E^{c'/b}_{a/c'} = \pm\epsilon_0$ we add only the contribution from the source(drain) contact where $|\mu_l - E^{c'/b}_{a/c'}| < W_{\rm e}$. Similarly, we find

$$\mathrm{Re}(\Sigma^{21}) - \mathrm{Re}(\Sigma^{21'}) = (1 + \bar\kappa_{\rm d} - \bar\kappa_\uparrow + \bar\kappa_\downarrow)\Psi^0_{\rm R}(\epsilon_0/2),$$

which leaves us with δ_1 from Eq. (17).

APPENDIX C: SPIN-ORBIT COUPLING AND VALLEY POLARIZATION

In Sec. III A, we discussed the possibility to include spin-orbit interaction effects, as they have been reported to play a prominent role in carbon nanotubes [38,40]. However, we did not add it in the comparison to the experimental data since they could not be resolved in the transport spectrum (Fig. 2).

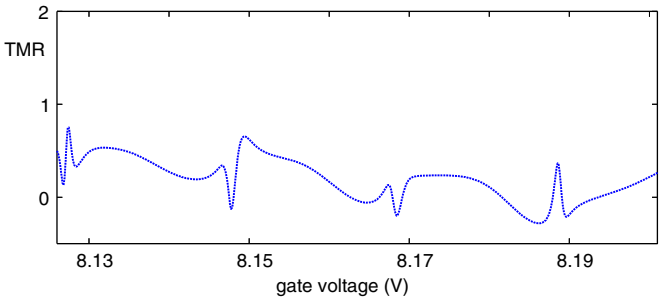

FIG. 13. (Color online) TMR as a function of gate voltage for orbital polarization $P_{\rm orb} = 0.6$, orbital shifts $g_{\rm orb}\mu_{\rm orb}h^{\rm orb}_{\rm ap} = -80$ μeV and $g_{\rm orb}\mu_{\rm orb}h^{\rm orb}_{\rm p} = -40$ μeV, and $\Delta_{\rm SO} = 0.1$ meV at $k_BT = 40$ μeV. The other parameters are identical to the ones used in Fig. 11.

Nevertheless, values of the order of $\Delta_{\rm SO} \sim 100$ μeV would still be consistent with the experimental data. Introducing a finite $\Delta_{\rm SO}$ *a priori* does not affect the TMR as the Kramers pairs are spin degenerate pairs with antiparallel and parallel alignment of spin and valley magnetic moments. Yet it has been argued that the two valleys of a CNT can couple differently to the leads [41]. If the valley quantum number is conserved upon tunneling, the mechanism can be understood in terms of a valley polarization. A possible tunneling Hamiltonian that describes this situation can be written as

$$\hat{\rm H}_{\rm T} = \sum_{l\mathbf{k}n\sigma\tau} T_{l\mathbf{k}n\sigma\tau} d^\dagger_{n\sigma\tau} c_{l\mathbf{k}\sigma} + \mathrm{H.c.}, \qquad \text{(C1)}$$

with a valley dependent coupling $T_{l\mathbf{k}n\sigma\tau}$ and an operator $c_{l\mathbf{k}\tau\sigma}$ that describes the electrons in the leads (that are also part of the CNT). Including a valley polarization in turn also renders the TMR sensitive to magnetic stray fields $g_{\rm orb}\mu_{\rm orb}h^{\rm orb}_{\rm p}$ and $g_{\rm orb}\mu_{\rm orb}h^{\rm orb}_{\rm ap}$ along the tube axis. The orbital magnetic moments $g_{\rm orb}\mu_{\rm orb}$ are considered to be larger then $\mu_{\rm B}$ by one order of magnitude [42]. In Fig. 13, we present a TMR calculation for $\Delta_{\rm SO} = 100$ μeV, orbital polarization $P_{\rm orb} = 0.6$ and stray fields $g_{\rm orb}\mu_{\rm orb}h^{\rm orb}_{\rm ap} = -80$ μeV and $g_{\rm orb}\mu_{\rm orb}h^{\rm orb}_{\rm p} = -40$ μeV again combined with the experimental data. The spin-dependent shifts are assumed to be negligible in this setup. We see that the agreement with the experimental data improved slightly in Fig. 13 at the expense of additional free parameters. It is, however, outside the scope of this paper to discuss the effect of spin-orbit coupling and the valley polarization in more detail.

[1] M. Zaffalon and B. J. van Wees, Phys. Rev. Lett. **91**, 186601 (2003).
[2] C.-M. Hu, J. Nitta, A. Jensen, J. B. Hansen, and H. Takayanagi, Phys. Rev. B **63**, 125333 (2001).
[3] L. Hofstetter, A. Geresdi, M. Aagesen, J. Nygård, C. Schönenberger, and S. Csonka, Phys. Rev. Lett. **104**, 246804 (2010).
[4] N. Tombros, C. Jozsa, M. Popinciuc, H. T. Jonkman, and B. J. van Wees, Nature (London) **448**, 571 (2007).
[5] A. N. Pasupathy, R. C. Bialczak, J. Martinek, J. E. Grose, L. A. K. Donev, P. L. McEuen, and D. C. Ralph, Science **306**, 86 (2004).
[6] M. M. Shulaker, G. Hills, N. Patil, H. Wei, H.-Y. Chen, H.-S. P. Wong, and S. Mitra, Nature (London) **501**, 526 (2013).
[7] S. Sahoo, T. Kontos, J. Furer, C. Hoffmann, M. Gräber, A. Cottet, and C. Schönenberger, Nat. Phys. **1**, 99 (2005).
[8] J.-R. Kim, H. M. So, J.-J. Kim, and J. Kim, Phys. Rev. B **66**, 233401 (2002).
[9] A. Jensen, J. R. Hauptmann, J. Nygård, and P. E. Lindelof, Phys. Rev. B **72**, 035419 (2005).
[10] B. Nagabhirava, T. Bansal, G. U. Sumanasekera, B. W. Alphenaar, and L. Liu, Appl. Phys. Lett. **88**, 023503 (2006).
[11] K. Tsukagoshi, B. W. Alphenaar, and H. Ago, Nature (London) **401**, 572 (1999).

[12] D. Orgassa, G. J. Mankey, and H. Fujiwara, Nanotechnol. **12**, 281 (2001).
[13] B. W. Alphenaar, K. Tsukagoshi, and M. Wagner, J. Appl. Phys. **89**, 6863 (2001).
[14] B. Zhao, I. Monch, T. Muhl, H. Vinzelberg, and C. M. Schneider, J. Appl. Phys. **91**, 7026 (2002).
[15] S. Chakraborty, K. M. Walsh, B. W. Alphenaar, L. Liu, and K. Tsukagoshi, Appl. Phys. Lett. **83**, 1008 (2003).
[16] W. Rudziński and J. Barnaś, Phys. Rev. B **64**, 085318 (2001).
[17] W. Wetzels, G. E. W. Bauer, and M. Grifoni, Phys. Rev. B **72**, 020407 (2005).
[18] S. Koller, L. Mayrhofer, and M. Grifoni, New J. Phys. **9**, 348 (2007).
[19] M. Braun, J. König, and J. Martinek, Phys. Rev. B **70**, 195345 (2004).
[20] A. Cottet and M.-S. Choi, Phys. Rev. B **74**, 235316 (2006).
[21] S. Koller, M. Grifoni, and J. Paaske, Phys. Rev. B **85**, 045313 (2012).
[22] J. Kern and M. Grifoni, Eur. Phys. J. B **86**, 384 (2013).
[23] R. López and D. Sánchez, Phys. Rev. Lett. **90**, 116602 (2003).
[24] J. Martinek, M. Sindel, L. Borda, J. Barnaś, J. König, G. Schön, and J. von Delft, Phys. Rev. Lett. **91**, 247202 (2003).
[25] M. Gaass, A. K. Hüttel, K. Kang, I. Weymann, J. von Delft, and C. Strunk, Phys. Rev. Lett. **107**, 176808 (2011).
[26] D. R. Schmid, S. Smirnov, M. Margańska, A. Dirnaichner, P. L. Stiller, M. Grifoni, A. K. Hüttel, and C. Strunk, Phys. Rev. B **91**, 155435 (2015).
[27] A. Cottet, T. Kontos, W. Belzig, C. Schönenberger, and C. Bruder, Europhys. Lett. **74**, 320 (2006).
[28] H. T. Man, I. J. W. Wever, and A. F. Morpurgo, Phys. Rev. B **73**, 241401(R) (2006).
[29] J. Barnaś and I. Weymann, J. Phys. Condens. Matter **20**, 423202 (2008).
[30] J. Samm, J. Gramich, A. Baumgartner, M. Weiss, and C. Schönenberger, J. Appl. Phys. **115**, 174309 (2014).
[31] M. Tolea, A. Aldea, and F. Tolea, Phys. Status Solidi B **243**, R84 (2006).
[32] J. V. Holm, H. I. Jørgensen, K. Grove-Rasmussen, J. Paaske, K. Flensberg, and P. E. Lindelof, Phys. Rev. B **77**, 161406 (2008).
[33] H. Aurich, A. Baumgartner, F. Freitag, A. Eichler, J. Trbovic, and C. Schönenberger, Appl. Phys. Lett. **97**, 153116 (2010).
[34] D. Choo, R. W. Chantrell, R. Lamberton, A. Johnston, and K. OGrady, J. Appl. Phys. **101**, 09E521 (2007).
[35] M. Dresselhaus, G. Dresselhaus, and P. Eklund, *Science of Fullerenes and Carbon Nanotubes: Their Properties and Applications* (Academic Press, Waltham, MA, 1996), p. 965.
[36] M. Marganska, P. Chudzinski, and M. Grifoni, arXiv:1412.7484.
[37] Y. Alhassid, T. Rupp, A. Kaminski, and L. I. Glazman, Phys. Rev. B **69**, 115331 (2004).
[38] F. Kuemmeth, S. Ilani, D. C. Ralph, and P. L. McEuen, Nature (London) **452**, 448 (2008).
[39] G. A. Steele, F. Pei, E. A. Laird, J. M. Jol, H. B. Meerwaldt, and L. P. Kouwenhoven, Nat. Commun. **4**, 1573 (2013).
[40] J. P. Cleuziou, N. V. N'Guyen, S. Florens, and W. Wernsdorfer, Phys. Rev. Lett. **111**, 136803 (2013).
[41] J. S. Lim, R. López, G. L. Giorgi, and D. Sánchez, Phys. Rev. B **83**, 155325 (2011).
[42] M. Rontani, Phys. Rev. B **90**, 195415 (2014).